24 Jun 2022

Carbon Nanotube Encapsulated Metal Selenide Nanostructures for Efficient Electrocatalytic Oxygen Evolution Reaction

Harish Singh

Wipula P.R. Liyanage

Manashi Nath
Missouri University of Science and Technology, nathm@mst.edu

Recommended Citation

Check for updates

Carbon nanotube encapsulated metal selenide nanostructures for efficient electrocatalytic oxygen evolution reaction†

Harish Singh, Wipula P. R. Liyanage and Manashi Nath ⓘ *

Nickel selenide nanowires were grown inside carbon nanotubes through *in situ* encapsulation *via* one-step chemical vapor deposition. These NiSe$_2$@CNT nanohybrids showed excellent electrocatalytic activity for water splitting with a low overpotential of 260 mV at 10 mA cm^{-2}, high current density, and extended stability owing to the synergistic effect between NiSe$_2$ and CNTs.

Rapid population growth on a global scale and over-exploitation of fossil fuels have intensified the importance of identifying renewable and environmentally friendly sustainable energy sources. Over the past several decades major efforts have been made to explore clean and sustainable alternative sources of energy to meet such rising energy demands and reduce the dependence on fossil fuel reserves. Among these, water electrolysis has been identified as an appealing technology for clean hydrogen generation, which can mitigate the increasing global energy demands. The efficiency of water electrolysis is restricted by the slow kinetics of electron-intensive oxygen evolution reaction (OER) at the anode. A high-performance electrocatalyst is required to accelerate the OER, lower overpotential, and maximize energy conversion.

Conventionally, state-of-the-art electrocatalysts for OER are mostly based on precious metal oxides, such as those of ruthenium (Ru) and iridium (Ir), although their widespread applications are hindered by scarcity and high cost.[1,2] In recent years, earth-abundant pyrite-type transition metal dichalcogenides (TMDs) with the general formula MX_2 (M = Co or Ni and X = Se or Te) have been identified as promising electrocatalysts for OER.[3,4] Ni has recently been utilized as an attractive element in the fabrication of anode materials for water electrolysis, due to low price, ample reserves, high electrochemical activity and durability in a highly alkaline medium.[5] Among various Ni-based compounds (*e.g.* oxides,[6]

hydroxides,[7,8] sulfides,[9] phosphides,[10] and nitrides[11]), nickel selenides have shown significant promise for OER due to their specific electronic structure, high electrical conductivity, low cost, and easy availability.[12] Various stoichiometries of nickel selenide have been explored as highly efficient OER electrocatalysts over the last few years. Nickel selenide can form with various stoichiometries, such as Ni$_{0.85}$Se/NiSe, NiSe$_2$, Ni$_3$Se$_4$, and Ni$_3$Se$_2$ each of which exhibits a unique lattice structure. Among these, NiSe$_2$ is of particular interest due to its intrinsic metallic properties and the enhanced electrochemical activity of the Ni center, making it a suitable electrocatalyst.[13] Unlike pyrites such as FeS$_2$ or NiS$_2$, NiSe$_2$ is a paramagnetic Pauli metal with a resistivity less than 10^{-3} cm.[14] Such high conductivity is very advantageous for OER activity since it improves charge transfer within the catalytic grains.

Apart from the high electrical conductivity of the catalyst grains, intergrain conductivity in the catalyst composite is also very crucial for improved electrocatalytic activity.[15–17] Moreover, poor electrical contact between the catalysts and electrode also leads to poor stability and the catalysts can be easily be peeled off during the oxygen evolution process. Hence, a common approach to increase the conductivity of the catalyst composite involves using conducting carbon nanostructures as an additive. In this regards, highly conductive multi-walled carbon nanotubes (MWCNTs) not only enable rapid charge transfer, but also provide routes for rapid ion transport and access to the electrolyte. Recently, Chen and co-workers have reported a series of studies on nickel selenide-CNT composites synthesised through a hydrothermal process that demonstrates surprisingly better performance for OER compared to support-free NiSe, NiSe$_2$ and Ni$_3$Se$_2$.[18] However higher onset potential of NiSe among all three nickel selenide catalysts limits the use of these composites for efficient fuel cell applications. Also, many advanced OER catalysts like these were synthesized using solvent-based hydrothermal techniques, which ultimately leads to secondary environmental pollution. In this communication we have reported a novel NiSe$_2$ nanorod encapsulated in MWCNT (NiSe$_2$@CNT) that was grown on a graphite foil substrate through a bottom-up method using a high-temperature

Department of Chemistry, Missouri University of Science and Technology, Rolla, MO, 65409, USA. E-mail: nathm@mst.edu
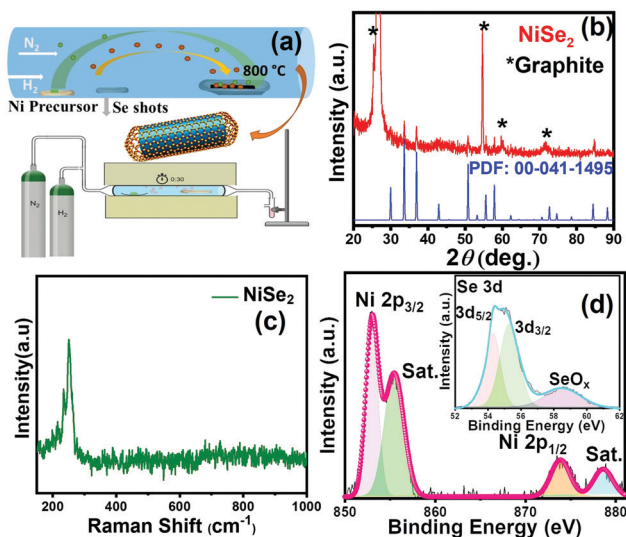
Fig. 1 (a) Synthesis scheme of NiSe$_2$@CNT on graphite foil through CVD and *in situ* encapsulation. (b) PXRD of as deposited NiSe$_2$@CNT on graphite foil. (c) Raman spectrum of as deposited NiSe$_2$@CNT. High resolution XPS spectra of (d) Ni and Se (inset).

CVD technique. This NiSe$_2$@CNT nanostructure exhibited highly efficient OER activity for extended time periods.

Volatile Ni-precursor, Ni-acetylacetonate and Se were used to grow the NiSe$_2$. Pyrolysis of the carbon-rich acetylacetonate ligand led to *in situ* growth of MWCNTs, while reaction between metal and selenium vapours led to the formation of metal selenide inside the growing nanotubes on the graphite foil substrate as shown in Fig. 1(a). Interestingly, acetylacetonate functions as an appropriate source of C without the need for using any other hydrocarbon precursor, which increases the purity of the product. It would be interesting to employ this kind of new synthesis strategy that would allow for extensive filling of the CNT channels with nanostructures, while also making it amenable to scale-up and improving reproducibility. The properties of carbon nanotubes are highly dependent on the structural characteristics of CNTs, such as their diameter, level of filling in the core, and the presence of defects. Three-dimensional (3D) structures would undoubtedly significantly increase the OER activity by exposing more accessible active sites from the external or inner surfaces.[19,20] CVD is a preferred and more efficient industrial technique for monitoring 2D and 3D nanomaterial growth and for modifying their properties as compared to other synthesis approaches. In addition, CVD is the most effective technique for homogeneous and continuous growth of thin films with very low defect density and high electro-conductivity.[21,22]

The PXRD patterns of the NiSe$_2$@CNT nanostructure hybrid showed characteristic diffraction peaks which matched well with the NiSe$_2$ standard diffraction pattern (PDF No. 00-041-1495) as shown in Fig. 1(b). The absence of PXRD peaks for metallic Ni or excess Se from the metal precursors used in the CVD process indicates the high purity of the as-grown NiSe$_2$ on the graphite foil substrate. Raman spectroscopy was used to examine the local structure of the as-prepared NiSe$_2$@CNT composite electrode (Fig. 1c), which confirmed the composition of the nanostructure hybrid. Raman peaks

were detected around 217 cm^{-1} and 243 cm^{-1}, corresponding to the A_g and T_g modes of NiSe$_2$, respectively.[23] Characteristic Raman peaks corresponding to MWCNTs were also observed at 1338 cm^{-1} (D-band) and 1584 cm^{-1} (G-band) as shown in Fig. S1 (ESI†). X-Ray photoelectron spectroscopy (XPS) was used to elucidate the chemical composition and changes in the electronic structure around the elements. Fig. 1d and Fig. S2 (ESI†) represent high resolution XPS spectra of Ni 2p, Se 3d and C1s, respectively. In Fig. 1d, the XPS spectra showed peaks at 856.8 and 874.6 eV corresponding to Ni 2p$_{1/2}$ and Ni 2p$_{3/2}$, respectively, and indicating the presence of Ni^{2+}. The peaks at 862.1 and 880.4 eV are ascribed to the satellite structures. The existence of Se^{2-} ions is supported by the two prominent peaks at 54.3 eV for Se 3d$_{5/2}$ and 55.2 eV for Se 3d$_{3/2}$. Furthermore, due to slight surface oxidation of Se, a shoulder peak was observed at 59.1 eV, which can be assigned to Se–O. The morphology of the NiSe$_2$@CNT nanostructure hybrid was studied with electron microscopy. Scanning electron microscopy (SEM) revealed a high yield of CNTs with length exceeding several micrometres, as illustrated in Fig. 2(a). The detailed morphology of the NiSe$_2$@CNT composite was studied through high-resolution transmission electron microscopy (HRTEM), which showed the extent of NiSe$_2$ filling within the MWCNTs as shown in Fig. 2(b–e). HRTEM images exhibited lattice fringes in the NiSe$_2$ filling with a layer spacing of 0.268 nm corresponding to (210) lattice planes of NiSe$_2$, indicating the high degree of crystallinity of the encapsulated NiSe$_2$ nanostructure. The average filling length of NiSe$_2$ was estimated to be in the range of 400–600 nm determined by studying several NiSe$_2$@CNT structures. It must be noted that TEM revealed the majority of the MWCNTs to be NiSe$_2$ filled.

The OER electrocatalytic performance of the as-prepared NiSe$_2$@CNT composite electrode (on graphite) was investigated in O$_2$-saturated 1 M KOH. Fig. 3(a) illustrates the LSV polarization curve of NiSe$_2$@CNT, which was compared with that of RuO$_2$. The LSV plots clearly showed that NiSe$_2$@CNT had better OER catalytic activity compared to RuO$_2$. Bare graphite foil and graphite foil heated at 800 °C were also studied as control substrates. As expected, the graphite foils did not show any activity for the OER, as shown in inset of Fig. 3(a), confirming that the observed activity for the composite electrode was due to the NiSe$_2$@CNT hybrid
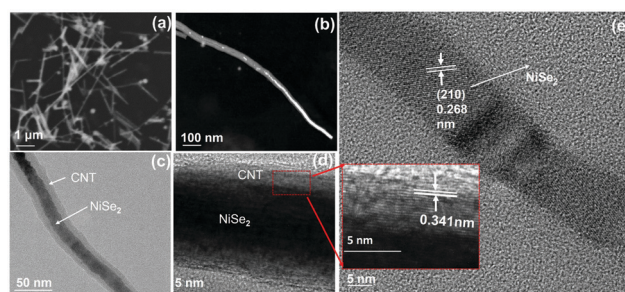
Fig. 2 (a) SEM of the NiSe$_2$@CNT electrode. (b) Dark field and (c) bright field TEM images of NiSe$_2$@CNT showing extensive filling. (d) TEM image of CNTs filled with NiSe$_2$ showing a diffused interface. (e) High-resolution TEM image showing the characteristic *d*-spacing of NiSe$_2$ in the core region and *d*-spacing of CNTs (inset, from region selected from (d)).
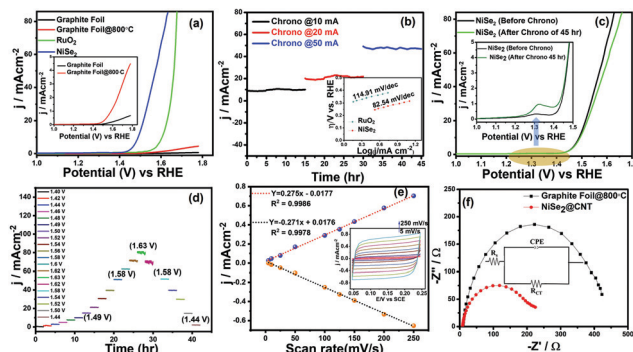
Fig. 3 OER electrocatalytic performance of NiSe$_2$@CNT. (a) LSVs measured in 1 M KOH at a scan rate of 10 mV s^{-1}. Inset illustrates the LSV polarization curves of bare graphite foil and graphite foil heated at 800 °C. (b) Chronoamperometry at different applied potentials. Inset shows the Tafel plots of NiSe$_2$@CNT and RuO$_2$. (c) LSVs of NiSe$_2$@CNT before and after 45 h of chronoamperometry. (d) Multistep chronoamperometry at different applied potential steps (ascending and descending). (e) Cyclic voltammograms measured at different scan rates for NiSe$_2$@CNT. Inset shows the anodic and cathodic currents measured as a function of different scan rates. (f) Nyquist impedance plots of NiSe$_2$@CNT. Inset represents the equivalent circuit model used for AC impedance fitting.

nanostructure. The effect of MWCNTs was also investigated by comparing the activity of NiSe$_2$@CNT with that of NiSe$_2$ synthesized through a hydrothermal method (NiSe$_2$-HD, characterized through PXRD as shown in Fig. S3 (ESI†), which showed peaks corresponding to pure NiSe$_2$, (PDF-00-041-1495)) and with that of commercially available MWCNTs. The results indicate that NiSe$_2$@CNT has the highest activity toward OER, requiring 260 mV overpotential to achieve a current density of 10 mA cm^{-2}, whereas NiSe$_2$-HD, RuO$_2$ and MWCNT required 300, 380 and 410 mV under similar conditions. As can be seen in Fig. S4 (ESI†), hydrothermally synthesized NiSe$_2$ and MWCNT samples showed higher onset potentials and lower conductivities than the CVD synthesized NiSe$_2$@CNT sample, which confirms the synergistic effect of the NiSe$_2$@CNT catalyst that was directly grown over the graphite foil, which produced a binder-free film. The hydrothermally synthesized NiSe$_2$ was assembled on the carbon cloth electrode by using Nafion as a binder, which limited the exposure of the active sites and introduced contact resistance between the electrode and catalysts, leading to subdued catalytic performance. Also, the as synthesized NiSe$_2$@CNT showed excellent catalytic activity as compared to most of the recently reported nickel-based catalysts (Table S1, ESI†). The OER kinetics were examined using the Tafel plots as shown in the inset of Fig. 3(b). Clearly, NiSe$_2$@CNT exhibited favourable OER kinetics, as measured by the small Tafel slope of 82.5 mV dec^{-1}, which was significantly less than that of the benchmark RuO$_2$ electrocatalyst (114.9 mV dec^{-1}). The lower Tafel slope of NiSe$_2$@CNT indicates a greater enhancement in OER kinetics since the current density increased steeply as the overpotential increased. A multistep chronoamperometry plot of the NiSe$_2$@CNT electrode is shown in Fig. 3(b), where the current density was increased sequentially from 10 to 50 mA cm^{-2} after every 15 hours, while the overpotential was measured at each constant current density. These chronoamperometry tests were performed at applied potentials of 1.49, 1.51 and 1.58 V to achieve a current density of 10, 20

and 50 mA cm^{-2}, respectively. NiSe$_2$@CNT demonstrated excellent stability at different applied potentials for prolonged times with minimal performance degradation as shown in Fig. 3(c), which revealed negligible shift in the polarization curves after 45 hours of multistep chronoamperometry, implying that the NiSe$_2$@CNT catalyst has exceptional mechanical robustness and mass transport capabilities for the OER under alkaline conditions. As shown in Fig. 3(d), multistep chronoamperometry measurements were also performed at various constant applied potentials to evaluate the robustness of the NiSe$_2$@CNT electrode. The potential steps were varied from 1.44 V to 1.62 V vs. RHE (ascending and descending) where the current density at each step was measured for ~2 h. Enhancement of the Ni oxidation peak was observed after long term chronoamperometry of NiSe$_2$@CNT composite electrodes as shown in the inset of Fig. 3(c). Such pre-oxidation has been observed commonly with the majority of Ni based electrocatalysts containing Ni^{2+} and attributed to local site oxidation of Ni(II) to Ni(III). Fig. 3(e) represents the ECSA of the as synthesised NiSe$_2$@CNT catalyst, wherein, higher ECSA values usually result in better active site exposure and OER catalysis. The ECSA of the NiSe$_2$@CNT electrode was obtained using the double layer capacitance in the non-faradaic region obtained from the cyclic voltammetry (CV) plots, as shown in the inset of Fig. 3(e). Corresponding capacitive currents at 0.15 V vs. SCE were recorded from each CV at different scan rates in 1 M KOH to determine the ECSA. The ECSA of the as prepared electrode was estimated to be 6.825 cm^2. The turnover frequency (TOF) of the NiSe$_2$@CNT sample was determined using a standard method as described in the ESI.† At a potential of 1.58 V and current density of 50 mA cm^{-2}, the TOF for NiSe$_2$@CNT was estimated to be 0.39 s^{-1}. Typically, higher TOF indicates improved catalytic activity, confirming the highly efficient electrocatalytic activity of the NiSe$_2$@CNT composite.[24,25] The faradaic efficiency of NiSe$_2$@CNT catalysts for OER activity was estimated to be 100% using the water displacement method. EIS measurements were used to determine the basis for the superior OER activity of the NiSe$_2$@CNT catalyst composite. The EIS plot (Fig. 3f) could be fitted to the equivalent circuit (Table S2, ESI†) and the charge-transfer resistance (R_{CT}) was estimated to be 209 Ω. Low R_{CT} for the NiSe$_2$@CNT composite compared to that of the bare graphite foil substrate heated at 800 °C (416 Ω) indicates facile charge transfer at the electrode–electrolyte interface due to the synergistic effect of the highly conductive NiSe$_2$@CNT electrode. The compositional stability of the catalyst was analyzed by measuring the XPS and Raman spectra after 45 hours of OER. The Raman spectrum (Fig. 4a) and XPS pattern (Fig. 4b) were found to be almost unchanged compared to those of the pristine sample indicating that the NiSe$_2$@CNT catalyst composite was indeed stable for extended periods.

The enhanced OER activity of the NiSe$_2$@CNT nanohybrid architecture indicates that the introduction of MWCNTs lowers the overpotential and can improve the electrical conductivity, which favours fast charge-transfer in the electrocatalytic process. Such intimate chemical fusion between the catalytic NiSe$_2$ and conducting MWCNT is more favourable than physical admixture (obtained by mixing NiSe$_2$ grains with MWCNTs), which shows reduced charge transfer across grain boundaries. The core–shell like NiSe$_2$@CNT nanohybrid, on the other hand, is expected to have
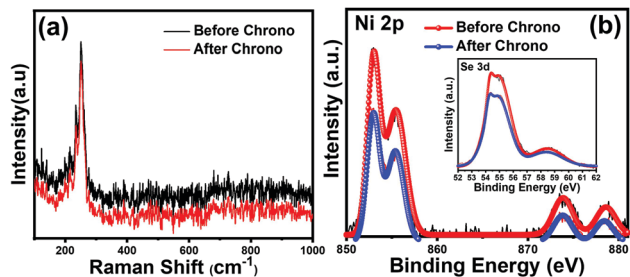
Fig. 4 (a) Raman and (b) XPS of NiSe$_2$@CNT after 45 h chronoamperometry.

enhanced charge transfer across the domain interface due to intermixing of the lattice planes at the interface (as seen in the TEM image, Fig. 2(d)), which is intrinsic to chemical fusion. Due to confinement effects induced by the surrounding CNT walls, it was inferred that NiSe$_2$ entrapped within the carbon nanotube channel not only exhibited outstanding catalytic performance but also showed superior stability under harsh oxidative conditions of water oxidation. The encapsulation of CNTs around metal chalcogenides is an intriguing concept that can increase conductivity and charge transfer, protect from catalyst leaching and peeling off and retain robust performance for maintaining steady catalytic efficiency.

In summary, the OER catalytic performance of NiSe$_2$@CNT was most strongly influenced by intergrowth of NiSe$_2$ within MWCNTs, synthesized by a CVD process. The NiSe$_2$@CNT nanohybrid also showed superior stability and significantly enhanced performance, with an overpotential of 260 mV at 10 mA cm^{-2} current density and a Tafel slope of 82.5 mV dec^{-1}. Additionally, this study establishes a new synthesis technique for designing nanohybrids with highly efficient metal chalcogenide nanorods wrapped within MWCNTs for fuel cell applications.

Conflicts of interest

There are no conflicts to declare.

Notes and references

1 T. Naito, T. Shinagawa, T. Nishimoto and K. Takanabe, *Inorg. Chem. Front.*, 2021, **8**, 2900–2917.
2 Y. Li, Y. Sun, Y. Qin, W. Zhang, L. Wang, M. Luo, H. Yang and S. Guo, *Adv. Energy Mater.*, 2020, **10**, 1903120.
3 M. Nath, U. De Silva, H. Singh, M. Perkins, W. P. R. Liyanage, S. Umapathi, S. Chakravarty and J. Masud, *ACS Appl. Energy Mater.*, 2021, acsaem.1c01438.
4 A. T. Swesi, J. Masud and M. Nath, *Energy Environ. Sci.*, 2016, **9**, 1771–1782.
5 K. S. Bhat and H. S. Nagaraja, *Mater. Res. Innovations*, 2019, **25**, 29–52.
6 A. G. Hufnagel, A. K. Henß, R. Hoffmann, O. E. O. Zeman, S. Häringer, D. Fattakhova-Rohlfing and T. Bein, *Adv. Mater. Interfaces*, 2018, **5**, 1–12.
7 M. Gao, W. Sheng, Z. Zhuang, Q. Fang, S. Gu, J. Jiang and Y. Yan, *J. Am. Chem. Soc.*, 2014, **136**, 7077–7084.
8 P. Ding, C. Meng, J. Liang, T. Li, Y. Wang, Q. Liu, Y. Luo, G. Cui, A. M. Asiri, S. Lu and X. Sun, *Inorg. Chem.*, 2021, **60**, 12703–12708.
9 O. Mabayoje, A. Shoola, B. R. Wygant and C. B. Mullins, *ACS Energy Lett.*, 2016, **1**, 195–201.
10 P. W. Menezes, A. Indra, C. Das, C. Walter, C. Göbel, V. Gutkin, D. Schmeißer and M. Driess, *ACS Catal.*, 2017, **7**, 103–109.
11 M. Shalom, V. Molinari, D. Esposito, G. Clavel, D. Ressnig, C. Giordano and M. Antonietti, *Adv. Mater.*, 2014, **26**, 1272–1276.
12 L. Lv, Z. Li, Y. Ruan, Y. Chang, X. Ao, J. G. Li, Z. Yang and C. Wang, *Electrochim. Acta*, 2018, **286**, 172–178.
13 M. Z. Xue and Z. W. Fu, *Electrochem. Commun.*, 2006, **8**, 1855–1862.
14 M. Z. Xue and Z. W. Fu, *Electrochem. Commun.*, 2006, **8**, 1855–1862.
15 A. Saxena, W. Liyanage, J. Masud, S. Kapila and M. Nath, *J. Mater. Chem. A*, 2021, **9**, 7150–7161.
16 X. Wang, A. Dong, Y. Hu, J. Qian and S. Huang, *Chem. Commun.*, 2020, **56**, 10809–10823.
17 L. Chai, Z. Hu, X. Wang, L. Zhang, T. T. Li, Y. Hu, J. Pan, J. Qian and S. Huang, *Carbon*, 2021, **174**, 531–539.
18 S. Chen, J.-L. Mi, P. Zhang, Y.-H. Feng, Y.-C. Yong and W.-D. Shi, *J. Phys. Chem. C*, 2018, **122**, 26096–26104.
19 T. Thippani, S. Mandal, G. Wang, V. K. Ramani and R. Kothandaraman, *RSC Adv.*, 2016, **6**, 71122–71133.
20 M. S. Ahmed, B. Choi and Y.-B. Kim, *Sci. Rep.*, 2018, **8**, 2543.
21 B. Liu, M. Fathi, L. Chen, A. Abbas, Y. Ma and C. Zhou, *ACS Nano*, 2015, **9**, 6119–6127.
22 S. Mishra, K. Song, K. C. Ghosh and M. Nath, *ACS Nano*, 2014, **8**, 2077–2086.
23 H. Zhou, Y. Wang, R. He, F. Yu, J. Sun, F. Wang, Y. Lan, Z. Ren and S. Chen, *Nano Energy*, 2016, **20**, 29–36.
24 Y. Qiu, X. Zhang, H. Han, Z. Liu, J. Liu and X. Ji, *J. Power Sources*, 2021, **499**, 229941.
25 Y. Qiu, Z. Feng, X. Ji and J. Liu, *Int. J. Hydrogen Energy*, 2021, **46**, 1501–1508.